Climate Feedbacks in CCSM3 under Changing CO_2 Forcing. Part II: Variation of Climate Feedbacks and Sensitivity with Forcing

ALEXANDRA K. JONKO AND KAREN M. SHELL

Oregon State University, Corvallis, Oregon

BENJAMIN M. SANDERSON AND GOKHAN DANABASOGLU

National Center for Atmospheric Research, Boulder, Colorado*

(Manuscript received 20 July 2012, in final form 13 October 2012)

ABSTRACT

Are equilibrium climate sensitivity and the associated radiative feedbacks a constant property of the climate system, or do they change with forcing magnitude and base climate? Using the radiative kernel technique, feedbacks and climate sensitivity are evaluated in a fully coupled general circulation model (GCM) for three successive doublings of carbon dioxide starting from present-day concentrations. Climate sensitivity increases by 23% between the first and third CO_2 doublings. Increases in the positive water vapor and cloud feedbacks are partially balanced by a decrease in the positive surface albedo feedback and an increase in the negative lapse rate feedback. Feedbacks can be decomposed into a radiative flux change and a climate variable response to temperature change. The changes in water vapor and Planck feedbacks are due largely to changes in the radiative response with climate state. Higher concentrations of greenhouse gases and higher temperatures lead to more absorption and emission of longwave radiation. Changes in cloud feedbacks are dominated by the climate response to temperature change, while the lapse rate and albedo feedbacks combine elements of both. Simulations with a slab ocean model (SOM) version of the GCM are used to verify whether an SOM-GCM accurately reproduces the behavior of the fully coupled model. Although feedbacks differ in magnitude between model configurations (with differences as large as those between CO_2 doublings for some feedbacks), changes in feedbacks between CO_2 doublings are consistent in sign and magnitude in the SOM-GCM and the fully coupled model.

1. Introduction

It has been suggested that climate sensitivity, Earth's equilibrium surface temperature response to an external perturbation, is a constant property of the climate system that remains unchanged under different forcing magnitudes and types. Indeed, several previous model studies find little to no dependence of climate sensitivity on forcing (Chen and Ramaswamy 1996; Forster et al. 2000; Boer and Yu 2003; Hansen et al. 2005). More recent work exploring a broader range of forcing (Boer et al. 2005; Colman and McAvaney 2009, hereafter CM09) suggests trends in climate sensitivity as external perturbations increase. However, these trends are not consistent among the studies, with each using different models, forcing agents, and methodologies.

CM09 use the partial radiative perturbation (PRP) method (Wetherald and Manabe 1988) to examine individual feedbacks in the Australian Bureau of Meteorological Research Centre (BMRC) atmospheric general circulation model (GCM) coupled to a mixed layer ocean model in response to CO_2 forcing ranging from $1/16$ to $32 \times$ present-day values. They find that while the radiative forcing increases with baseline CO_2 amount, climate sensitivity decreases, and they identify a reduced albedo feedback as the main source of this decrease.

Boer et al. (2005) employ changes in solar constant as a forcing analog to CO_2 changes to investigate the response of climate sensitivity in the National Center for Atmospheric Research (NCAR) Climate System Model

* The National Center for Atmospheric Research is sponsored by the National Science Foundation.

Corresponding author address: Alexandra K. Jonko, College of Earth, Ocean and Atmospheric Sciences, Oregon State University, 104 CEOAS Admin. Bldg., Corvallis, OR 97331-5503.
E-mail: ajonko@coas.oregonstate.edu

DOI: 10.1175/JCLI-D-12-00479.1

(CSM) and detect an increase in climate sensitivity with increasing forcing for solar constant changes up to 25%. For larger changes, they observe a runaway effect associated with cloud changes and the shortwave (SW) cloud feedback in particular.

Both of these studies, like most work investigating the relationship between climate sensitivity and forcing, use atmospheric general circulation models (AGCMs) coupled to a slab ocean model (SOM). Simulations with this setup equilibrate quickly, even for very large perturbations. However, they do not permit the role of the ocean circulation to be taken into account explicitly. As pointed out by CM09, similar analyses with fully coupled models are required to confirm that SOMs can adequately represent ocean processes relevant to climate sensitivity.

Hansen et al. (2005) investigate the role of the ocean component of a coupled model by comparing climate sensitivity estimates obtained with the Goddard Institute for Space Studies (GISS) Model E coupled to several different ocean models. They obtain comparable estimates of climate sensitivity for three ocean models of different complexity. However, the dynamic model they use is somewhat simplified (Russell et al. 1995) and results for a fully dynamic model are not presented.

Danabasoglu and Gent (2009) compare equilibrium climate sensitivity in the fully coupled NCAR Community Climate System Model version 3 (CCSM3) to its slab ocean version for an instantaneous doubling of CO_2 concentrations and find that sensitivities are comparable within an uncertainty range defined based on interannual variability. Here we extend their analysis by including simulations with larger forcing and by evaluating individual feedbacks in addition to climate sensitivity. We add two simulations forced with 4 and 8 times present-day CO_2 concentrations. The range of forcing we are able to explore is limited compared to CM09, since the fully coupled model takes a much longer time to adjust to an imposed perturbation and therefore is much more costly to run.

We evaluate climate sensitivity and feedbacks for each of the three doublings of CO_2 concentrations ($2xCO_2$-$1xCO_2$, $4xCO_2$-$2xCO_2$, and $8xCO_2$-$4xCO_2$) using the radiative kernel technique extended for large nonlinear perturbations (Jonko et al. 2012). Additionally, we compare feedbacks and climate sensitivity estimates from CCSM and its atmospheric component, the Community Atmosphere Model version 3, coupled to a slab ocean model (CAM-SOM), to evaluate the accuracy of the slab ocean model for feedback estimates. In the next section, we present the model data used in our analysis. Section 3 explains the methods used and gives an overview of the order in which results will be presented. The impact of varying forcing on individual feedbacks and climate sensitivity is discussed in sections 4 and 5, respectively. Results are summarized in section 6.

2. Model data

We analyze four simulations of the low-resolution NCAR CCSM3, truncated at T31 with 26 vertical levels (Yeager et al. 2006), for both the full depth ocean (CCSM) and the slab ocean (CAM-SOM) configurations. Included are a control run with 1990 CO_2 concentrations of 355 ppmv and simulations in which these concentrations were doubled to 710 ppmv, quadrupled to 1420 ppmv, and octupled to 2840 ppmv, respectively.

Figures 1a and 1b show global average changes in net top-of-atmosphere (TOA) flux (absorbed solar minus outgoing longwave radiation) between the three perturbed simulations and the control run for CCSM and CAM-SOM. While all CAM-SOM simulations were run for 60 years, the CCSM $2xCO_2$ simulation was run for 3000 years—the time scale for adjustment of the deep ocean (Danabasoglu 2004; Stouffer 2004)—and the $4xCO_2$ and $8xCO_2$ simulations were stopped after 2000 and 1450 years, respectively. Years 1 to 1450 are shown for all three cases. In the $2xCO_2$ simulation, the climate system reaches equilibrium with respect to the applied forcing after approximately 2000 years. For comparison, all three perturbed CAM-SOM simulations reach equilibrium after approximately 25 to 30 years. For the larger $4xCO_2$ and $8xCO_2$ perturbations, the time scale of equilibration for CCSM is longer. Hence, the $4xCO_2$ and $8xCO_2$ simulations are not in equilibrium at the end of the simulations. The remaining net TOA flux imbalance, computed from the average over the last common decade of the simulations 1441 to 1450, increases from 0.14 W m^{-2} for $2xCO_2$ to 0.59 W m^{-2} for $8xCO_2$. Figures 1c and 1d show the surface air temperature change for each doubling in CO_2 concentration. We are interested in the temperature change per doubling of CO_2, rather than the change from the control run, because changes in this value indicate deviations from linearity in the behavior of the system for successive CO_2 doublings. In both model versions the temperature change at year 1450 increases in magnitude from 2.2 K for the first doubling to 3.2 K for the third doubling, an increase of 1 K.

In CCSM, the global mean surface air temperature increases by 2.2 K in $2xCO_2$, 4.7 K in $4xCO_2$, and by 7.9 K in $8xCO_2$ relative to the control run for each forced simulation by the last common decade of the simulations. For comparison, the equilibrium temperature increase in the $2xCO_2$ simulation totals 2.5 K (based on model years 2991–3000). Values in CAM-SOM for the last decade of the simulations (model years 51–60) are almost identical at 2.2, 4.7, and 7.8 K.

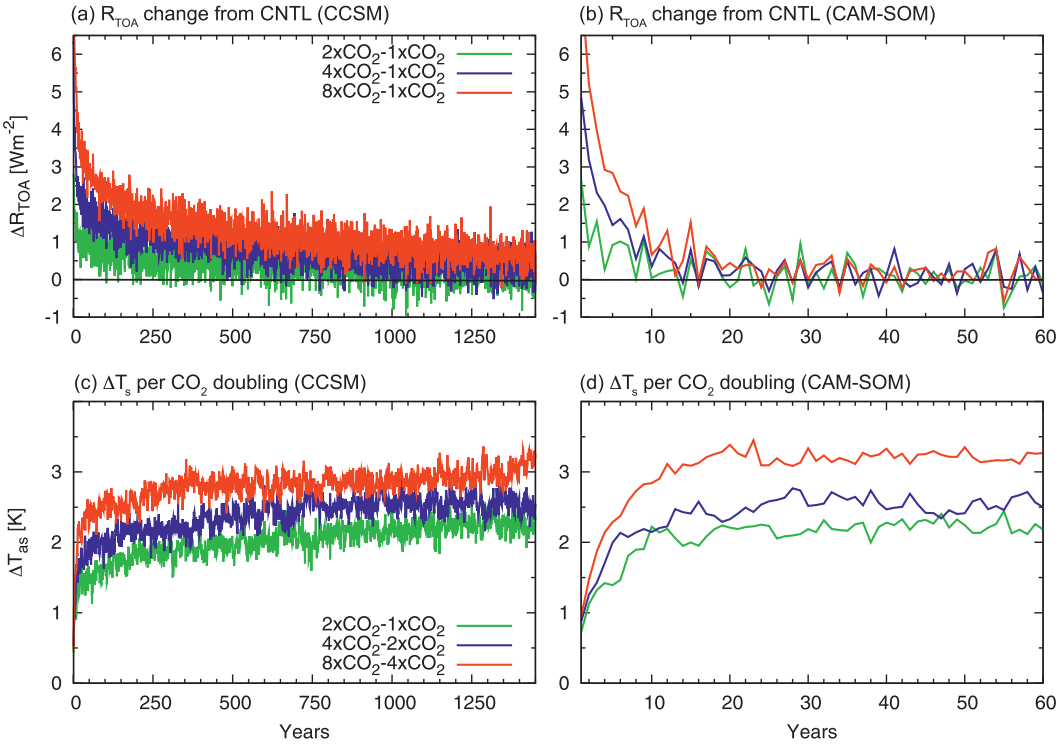

FIG. 1. (a),(b) Global, annual average difference (W m^{-2}) in TOA net radiative flux (absorbed SW radiation − outgoing LW radiation) between each perturbed simulation and the unforced control run, representing the flux imbalance at the top of the atmosphere in the perturbed simulations, for (a) CCSM and (b) CAM-SOM. (c),(d) As in (a),(b), but for global, annual average change (K) in surface air temperature for each CO_2 doubling.

3. Methods

The final equilibrium temperature change in response to a forcing depends not only on the forcing F itself, but also on the magnitude of the feedback parameter λ:

$$F = -\frac{\Delta R}{\Delta \overline{T}_{\rm as}} \Delta \overline{T}_{\rm as} = -\lambda \Delta \overline{T}_{\rm as}. \qquad (1)$$

Here, R is the net radiative flux (excluding the forcing), $\Delta \overline{T}_{\rm as}$ is the global average change in surface air temperature, and λ is the feedback parameter containing contributions from individual feedback processes related to the Planck response (P) as well as changes in lapse rate (LR), specific humidity (q), surface albedo (α), and clouds (C):

$$\lambda = \lambda_P + \lambda_{\ln(q)} + \lambda_{\rm LR} + \lambda_\alpha + \lambda_C + {\rm Re}, \qquad (2)$$

where $\ln(q)$ is the natural logarithm of specific humidity, used to evaluate the water vapor feedback, and Re is a residual, containing higher-order cross terms and is relatively small (about 10%; Jonko et al. 2012). We use the radiative kernel technique (Shell et al. 2008; Soden et al. 2008; Jonko et al. 2012) to calculate individual feedbacks. It has been shown that this linear technique in its original form is valid for small perturbations on the order of $2xCO_2$ (Jonko et al. 2012). Since we are dealing with much larger forcings here, we use a combination of kernels, based on different climate states, which is more suitable for large nonlinear perturbations: a present-day ($1xCO_2$) base kernel for $2xCO_2$-$1xCO_2$ feedbacks, an $8xCO_2$ base kernel for $8xCO_2$-$4xCO_2$ feedbacks, and a combination of both (½$1xCO_2$ kernel + ½$8xCO_2$ kernel) for $4xCO_2$-$2xCO_2$ feedbacks.

To calculate the water vapor and albedo feedbacks we simply multiply the appropriate kernels by differences in feedback variable between experiment and control simulations, normalized by global average surface air temperature change, $d\overline{T}_{\rm as}$:

$$\lambda_X = \frac{\partial R}{\partial X} \frac{dX}{d\overline{T}_{\rm as}}, \qquad (3)$$

where X stands for the feedback variables, the natural log of specific humidity and surface albedo.

The Planck feedback is the response of longwave (LW) TOA flux to a perturbation in surface temperature that is applied to each vertical layer of the troposphere.

It is the sum of the atmospheric temperature kernel at every level of the troposphere and the surface temperature kernel, both multiplied by the surface temperature change and normalized by $d\overline{T}_{\rm as}$:

$$\lambda_P = \frac{\partial R}{\partial T_s}\frac{dT_s}{d\overline{T}_{\rm as}} + \frac{\partial R}{\partial T}\frac{dT_s}{d\overline{T}_{\rm as}}. \quad (4)$$

The lapse rate feedback is the radiative response to changing vertical temperature structure and is computed by taking the difference between the atmospheric temperature feedback and the second term of the Planck feedback:

$$\lambda_{\rm LR} = \frac{\partial R}{\partial T}\frac{dT}{d\overline{T}_{\rm as}} - \frac{\partial R}{\partial T}\frac{dT_s}{d\overline{T}_{\rm as}}. \quad (5)$$

Because of nonlinearities introduced primarily by cloud overlap, the evaluation of the cloud feedback using a cloud kernel is less straightforward. Zelinka et al. (2012) and Sanderson and Shell (2012) have calculated cloud kernels. However, such computations require the use of output from a cloud simulator, which is not available for the simulations used here. Rather, we employ the concept of cloud radiative forcing (CRF), defined as the difference between all-sky and clear-sky fluxes ($R' - R'_c$) (Cess and Potter 1987). Note that R' differs from R in Eq. (3) in that it does include the forcing, F. CRF measures the effect of clouds on the radiation budget for a given climate state. The change in CRF due to an external forcing is often used to approximate the cloud feedback (Soden et al. 2004):

$$\Delta{\rm CRF} = \Delta(R' - R'_c). \quad (6)$$

The quantity ΔCRF is a biased estimator of cloud feedback because of its sensitivity not only to cloud changes, but also to changes in noncloud variables (Soden et al. 2004, 2008). Using the kernel technique, ΔCRF can be corrected for such biases by subtracting from it the differences between all-sky and clear-sky feedbacks:

$$\Delta{\rm CRF}_k = \Delta[(R - R_c)_P + (R - R_c)_{\ln(q)} + (R - R_c)_{\rm LR} + (R - R_c)_\alpha + (F - F_c)_{\rm CO_2}]. \quad (7)$$

Here, $(F - F_c)_{\rm CO_2}$ is the difference between the all-sky and clear-sky CO_2 forcing. While ΔCRF alone is small and negative in CCSM3, the adjusted ΔCRF is positive and substantially larger in magnitude, illustrating the large bias of ΔCRF due to changes in noncloud feedbacks. To obtain a cloud feedback, the adjusted ΔCRF ($=\Delta{\rm CRF} - \Delta{\rm CRF}_k$) is normalized by $\Delta\overline{T}_{\rm as}$.

Other decompositions are equally valid. For example, Zhang et al. (1994) use surface and atmospheric temperature as feedback variables rather than the Planck response and lapse rate. The radiative kernel technique is not as accurate as the PRP method used by CM09. However, it would be impractical to use PRP here, since it requires a set of radiative transfer calculations to be carried out for each feedback estimate.

We compare feedbacks for three successive doublings in CO_2 concentration: 355 to 710 ppmv ($2xCO_2$-$1xCO_2$), 710 to 1420 ppmv ($4xCO_2$-$2xCO_2$), and 1420 to 2840 ppmv ($8xCO_2$-$4xCO_2$). For CAM-SOM simulations we use 30-yr averages of model variables over the years 31 to 60, while 100 30-yr means (running averages separated by 10-yr intervals) from years 431 through 1450 are used for feedback estimates from CCSM simulations. For CCSM feedbacks, Fig. 2 shows histograms of global, annual 30-yr average values for the three doublings, binned using 0.01 W m^{-2} K^{-1} intervals. Also shown are the overall 1000-yr averages (squares) and standard deviations (error bars), a measure of the uncertainty in the estimate of the mean due to interannual and other short-term variability. Overall averages are compared with CAM-SOM average feedbacks in Table 1, while differences between doublings are summarized in Table 2.

We assess the statistical significance of the differences between the feedback distributions using recurrence analysis (von Storch and Zwiers 1988). Rather than testing for differences between sample means, this method evaluates the degree of separation between two sample distributions. Two random variables are said to be (p, q) recurrent if q percent of the probability density function of one variable lies outside of p percent of the distribution of the other variable. Thus, sample means of two random variables that are (50%, 84%) recurrent are separated by one standard deviation (von Storch and Zwiers 1988; see their Fig. 4). A nonparametric method to test for recurrence involves counting the number of realizations of one random variable that lie beyond a threshold, defined as a percentile of the normal distribution fitted to the other variable. The most robust such test is to reject the null hypothesis of a realization not being attributable to one or the other distribution if the smallest realization of one distribution is larger than the largest realization of the other (i.e., there is no overlap between distributions). This is the case for all differences between CO_2 doublings for water vapor and albedo feedbacks and climate sensitivity (Figs. 2b,d,h), as well as some of the differences in Planck, SW cloud, and net cloud feedbacks (Figs. 2a,e,g). For these cases we reject the null hypothesis and infer that the feedback distributions are significantly different. For the remaining cases, we test for (50%, 98%) recurrence, which represents

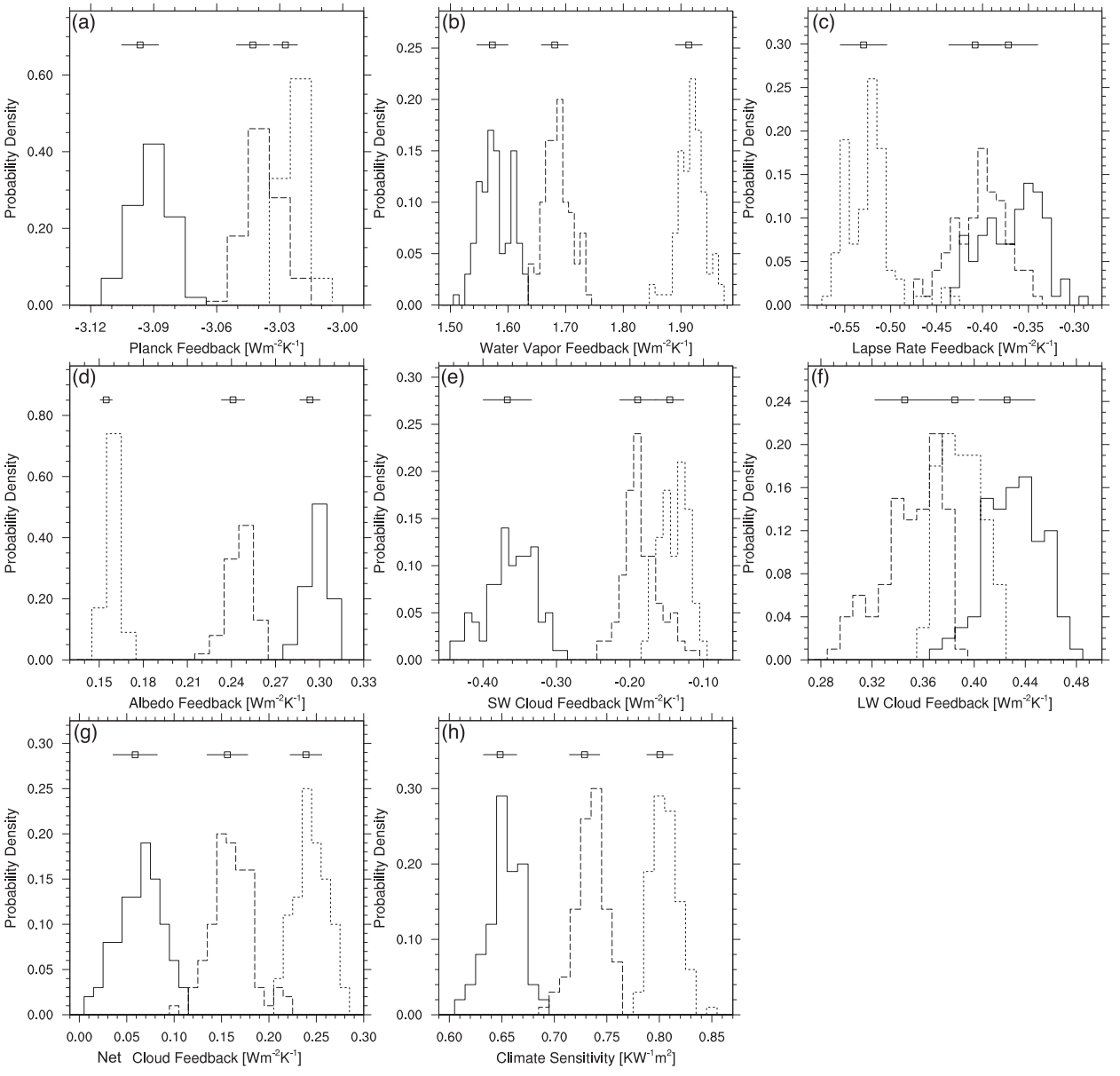

FIG. 2. Normalized histograms of feedbacks and climate sensitivity, binned using an interval of 0.01, for the three CO_2 doublings for 30-yr running averages, separated by 10 years, for model years 431–1450. Solid lines: $2xCO_2$-$1xCO_2$; long dashed lines: $4xCO_2$-$2xCO_2$; short dashed lines: $8xCO_2$-$4xCO_2$. Boxes above the histograms represent sample means, and error bars to either side of boxes are standard deviations: (a) Planck, (b) water vapor, (c) lapse rate, (d) albedo, (e) SW cloud, (f) LW cloud, (g) net cloud feedbacks, and (h) climate sensitivity.

a separation of means by two standard deviations. We fit a normal distribution to the feedback distribution with the smaller average value and find its 98th percentile X_p. We then count the realizations of the other feedback distribution that are larger than this threshold. If the count T equals the sample size $n = 100$, the difference between feedbacks is found to be (50%, 98%) recurrent at significance level $q^n = 0.98^{100} = 0.13$, or 87% (X_p and T are summarized in Table 3).

Because we are using a different kernel for each CO_2 doubling, we can separate the change in feedbacks between CO_2 doublings into a radiative response (changes in kernels) and a climate response (changes in feedback variables as a function of surface air temperature change).

While we can track the change in surface temperature and feedback variables, $dX/d\overline{T}_{as}$, over the course of the coupled model runs, we only have one estimate of the kernel $\delta R/\delta X$ in each case. Hence, the variability in

TABLE 1. Feedbacks in units of W m^{-2} K^{-1} in (a) CCSM and (b) CAM-SOM for the $2xCO_2$-$1xCO_2$, $4xCO_2$-$2xCO_2$, and $8xCO_2$-$4xCO_2$ experiments computed from 1000-yr averages (years 451–1450) using $1xCO_2$, average, and $8xCO_2$ kernels (k), compared to "hybrid" feedbacks computed combining the $8xCO_2$ kernel with the $2xCO_2$-$1xCO_2$ climate response and the $1xCO_2$ kernel with the $8xCO_2$-$4xCO_2$ climate response; s is the climate sensitivity in units of K (W m^{-2})$^{-1}$.

(a) CCSM	Planck	ln(q)	LR	α	SW C	LW C	Net C	s
$2xCO_2$-$1xCO_2$ ($1xCO_2$ k)	−3.10	1.57	−0.37	0.29	−0.37	0.43	0.06	0.65
$4xCO_2$-$2xCO_2$ (avg. k)	−3.04	1.68	−0.41	0.24	−0.19	0.35	0.16	0.73
$8xCO_2$-$4xCO_2$ ($8xCO_2$ k)	−3.03	1.91	−0.53	0.16	−0.15	0.39	0.24	0.80
$2xCO_2$-$1xCO_2$ ($8xCO_2$ k)	−3.00	1.84	−0.39	0.26	−0.40	0.47	0.07	0.82
$8xCO_2$-$4xCO_2$ ($1xCO_2$ k)	−3.13	1.64	−0.49	0.25	−0.18	0.34	0.16	0.64
(b) CAM-SOM	Planck	ln(q)	LR	α	SW C	LW C	Net C	s
$2xCO_2$-$1xCO_2$ ($1xCO_2$ k)	−3.10	1.64	−0.48	0.26	−0.39	0.44	0.05	0.61
$4xCO_2$-$2xCO_2$ (avg. k)	−3.06	1.80	−0.56	0.18	−0.31	0.43	0.12	0.66
$8xCO_2$-$4xCO_2$ ($8xCO_2$ k)	−3.03	2.03	−0.65	0.09	−0.19	0.49	0.30	0.79
$2xCO_2$-$1xCO_2$ ($8xCO_2$ k)	−3.00	1.94	−0.48	0.18	−0.38	0.51	0.13	0.81
$8xCO_2$-$4xCO_2$ ($1xCO_2$ k)	−3.13	1.74	−0.60	0.15	−0.20	0.45	0.25	0.63

feedback values shown in the individual histograms (Fig. 2) reflects only the temporal evolution of feedback variable and surface temperature changes, not changes in the radiative flux response.

To evaluate whether the changes in feedbacks between the individual doublings are due to changes in the radiative or climate response, we compute "hybrid feedbacks," combining the $8xCO_2$ kernel with the $2xCO_2$-$1xCO_2$ climate response and the $1xCO_2$ kernel with the $8xCO_2$-$4xCO_2$ climate response, and compare these with the "full" $2xCO_2$-$1xCO_2$ and $8xCO_2$-$4xCO_2$ feedbacks in Table 1. The differences between feedbacks for the first and third CO_2 doubling are compared with differences between the full $2xCO_2$-$1xCO_2$ feedback and the hybrid feedbacks in Table 2. Zonal distributions of full and hybrid feedbacks are investigated in Fig. 3. The kernels used are represented by line type (solid or dashed), while the climate response is represented by line color. Thus, solid blue lines are full $2xCO_2$-$1xCO_2$ feedbacks and the dashed red lines are full $8xCO_2$-$4xCO_2$ feedbacks, while the dashed blue lines are hybrid feedbacks computed combining $2xCO_2$-$1xCO_2$ climate responses with $8xCO_2$ kernels and solid red lines are hybrid feedbacks that result from the combination of $8xCO_2$-$4xCO_2$ climate responses and $1xCO_2$ kernels. When lines of the same color lie close together, this means that changing the kernel does not impact the feedback. When lines of the same type overlap, it follows that feedbacks are insensitive to changing climate responses. While the figures and tables introduced here contain results for all feedbacks, we will examine each of the feedbacks individually, making reference to the appropriate locations in each figure and table, throughout the following sections.

4. Radiative feedbacks

a. Planck feedback

Increasing temperatures at the surface and throughout the atmosphere lead to an increase in outgoing LW radiation, which stabilizes the climate system. The Planck feedback is defined as the response of LW TOA flux to the perturbation in surface temperature applied to each vertical layer of the troposphere. It is the strongest

TABLE 2. Differences between $2xCO_2$-$1xCO_2$ and $8xCO_2$-$4xCO_2$ feedbacks and climate sensitivity in (a) CCSM and (b) CAM-SOM. The total difference (between the first and third rows in Tables 1a and 1b), as well as contributions to it from changes only in the kernel (difference between the first and forth rows in Tables 1a and 1b) and changes only in the climate response (difference between the first and fifth rows in Tables 1a and 1b) are shown.

(a) CCSM	Planck	ln(q)	LR	α	SW C	LW C	Net C	s
Total difference	0.07	0.34	−0.16	−0.13	0.22	−0.04	0.18	0.15
due to kernel	0.10	0.27	−0.02	−0.03	−0.03	0.04	0.01	0.17
due to climate response	−0.03	0.07	−0.12	−0.04	0.19	−0.09	0.10	−0.01
(b) CAM-SOM	Planck	ln(q)	LR	α	SW C	LW C	Net C	s
Total difference	0.07	0.39	−0.17	−0.17	0.20	0.05	0.25	0.18
due to kernel	0.10	0.30	0.00	−0.08	0.01	0.07	0.08	0.20
due to climate response	−0.03	0.10	−0.12	−0.11	0.19	0.01	0.20	0.02

TABLE 3. Results of recurrence analysis for those feedbacks that show overlap between histograms; X_p is the 98th percentile of the feedback distribution with the smaller mean and T is the test statistic (i.e., the count of realizations from the sample with the larger mean that are larger than X_p). When T equals the sample size $n = 100$, the difference between feedbacks is found to be (98%, 50%) recurrent at significance level $q^n = 0.98^{100} = 0.13$.

Feedback pair	X_p	T
Planck feedback (second to third doubling)	−3.027	45
Lapse rate feedback (second to first doubling)	−0.349	28
Lapse rate feedback (third to first doubling)	−0.477	100
Lapse rate feedback (third to second doubling)	−0.477	100
SW cloud feedback (second to third doubling)	−0.139	42
LW cloud feedback (second to first doubling)	0.394	94
LW cloud feedback (third to first doubling)	0.416	67
LW cloud feedback (second to third doubling)	0.394	29
Net cloud feedback (first to second doubling)	0.107	100
Net cloud feedback (second to third doubling)	0.200	100

negative feedback, with an average value that decreases in magnitude slightly from −3.10 to −3.03 W m^{-2} K^{-1} between the first and third CO_2 doubling in both CCSM (Fig. 2a) and CAM-SOM. The larger change occurs between the first and second doublings in CO_2, showing no overlap between distributions, while the change between the second and third doublings is rather small and not found to be significant by the recurrence test (Table 3). The decrease reflects changes in surface and atmospheric temperature kernels (Jonko et al. 2012), or the radiative response (Tables 1 and 2), since the climate response for the Planck feedback is $dT_s/d\overline{T}_{as} \approx 1$.

Thus, in a warmer climate with higher concentrations of LW absorbers, the change in OLR for a standard temperature anomaly decreases.

b. Water vapor feedback

As atmospheric temperatures rise, so does the water vapor content of the atmosphere, strengthening the greenhouse effect and resulting in a positive water vapor feedback. This feedback, $[\partial R/\partial \ln(q)][d\ln(q)/d\overline{T}_{as}]$, is calculated using the change in the natural logarithm of specific humidity, since absorption of radiation by water vapor scales approximately linearly with the natural logarithm rather than the absolute value of specific humidity (Raval and Ramanathan 1989). The water vapor feedback is strongest in the tropics, where the troposphere is close to saturation, but it is positive everywhere (Fig. 3b). It increases with baseline CO_2 concentration, from 1.57 to 1.91 W m^{-2} K^{-1} in CCSM. All differences are found to be significant (i.e., there is no overlap between histograms in Fig. 2b). For CAM-SOM the feedback increases from 1.64 to 2.03 W m^{-2} K^{-1} (Table 1). Since the kernel and global average surface air temperature changes are the same for both CCSM and CAM-SOM, the larger feedback in CAM-SOM is related to a stronger increase in specific humidity in this configuration. The increase in feedback with CO_2 baseline amount is explained primarily by an increase in radiative kernel $\partial R/\partial \ln(q)$ (lines of the same type lie close together in Fig. 3b) since, for every CO_2 doubling, higher concentrations not only of water vapor but also of CO_2 increase the rate of absorption of LW radiation (Jonko et al. 2012). The climate response remains approximately constant, increasing only slightly for successive doublings of CO_2 and accounting for roughly 20% (CCSM) and 25% (CAM-SOM) of the water vapor feedback increase (Table 2).

c. Lapse rate feedback

The lapse rate feedback measures the impact of a radiative perturbation on the vertical structure of atmospheric temperature. The strongest contributions to this feedback stem from the radiative effect of a decreasing moist adiabatic lapse rate with surface temperature warming that occurs over areas where the troposphere is near saturation. This is the case in much of the tropics. Since a smaller lapse rate translates into a stronger warming in the upper troposphere and increased upwelling LW radiation from these levels, the lapse rate feedback is negative in the tropics (Fig. 3c). The decrease in lapse rate is a function of the initial surface temperature as well as the temperature change, and the lapse rate feedback increases in magnitude with each CO_2 doubling along with the starting surface temperature, from −0.37 to −0.53 W m^{-2} K^{-1} in CCSM. 75% of this increase is explained by the climate response, with only a small portion coming from radiative kernel changes. Figure 3c shows that the lapse rate feedback at all latitudes is shifted toward more negative values with increasing baseline CO_2 amount. In the tropics, this increase in negative feedback values is due primarily to changes in radiative kernel. Here lines of the same type overlap in Fig. 3c. In the extratropics, however, the decrease in positive values stems mostly from changes in the surface and atmospheric temperature responses, and lines of the same color lie closer together in Fig. 3c.

Histograms for the lapse rate feedback exhibit the largest overlap of all feedbacks, in particular between the first and second CO_2 doubling (Fig. 2c). The separation between these two distributions is not found to be recurrent, unlike the differences between the first and third doublings, as well as the second and third doublings, which are recurrent.

Compared with CCSM, CAM-SOM has a stronger lapse rate feedback, which increases in magnitude from −0.48 to −0.65 W m^{-2} K^{-1} for the first and third CO_2 doublings, respectively. Note that the difference between CAM-SOM and CCSM feedbacks for individual CO_2

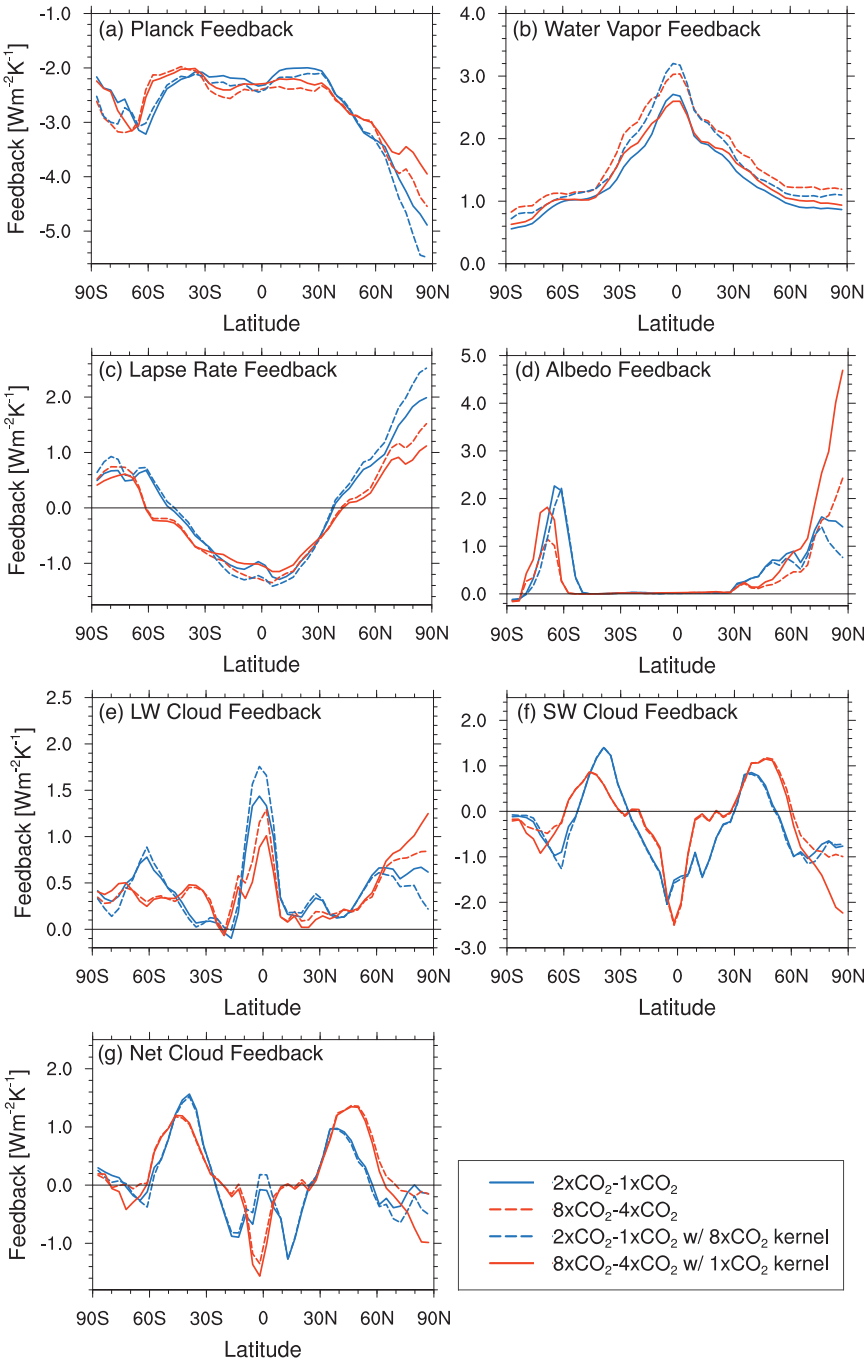

FIG. 3. Zonal distributions of 1000-yr average CCSM feedbacks. Solid blue lines: full $2xCO_2$-$1xCO_2$ feedbacks; dashed red lines: full $8xCO_2$-$4xCO_2$ feedbacks; dashed blue lines: hybrid feedbacks with $2xCO_2$-$1xCO_2$ climate response and $8xCO_2$ kernel; solid red lines: hybrid feedbacks $8xCO_2$-$4xCO_2$ climate response and $1xCO_2$ kernel. Feedbacks computed using the same kernel are represented by lines of the same type, while feedbacks computed using the same climate response are represented by lines of the same color: (a) Planck, (b) water vapor, (c) lapse rate, (d) albedo, (e) LW cloud, (f) SW cloud, and (g) net cloud feedbacks.

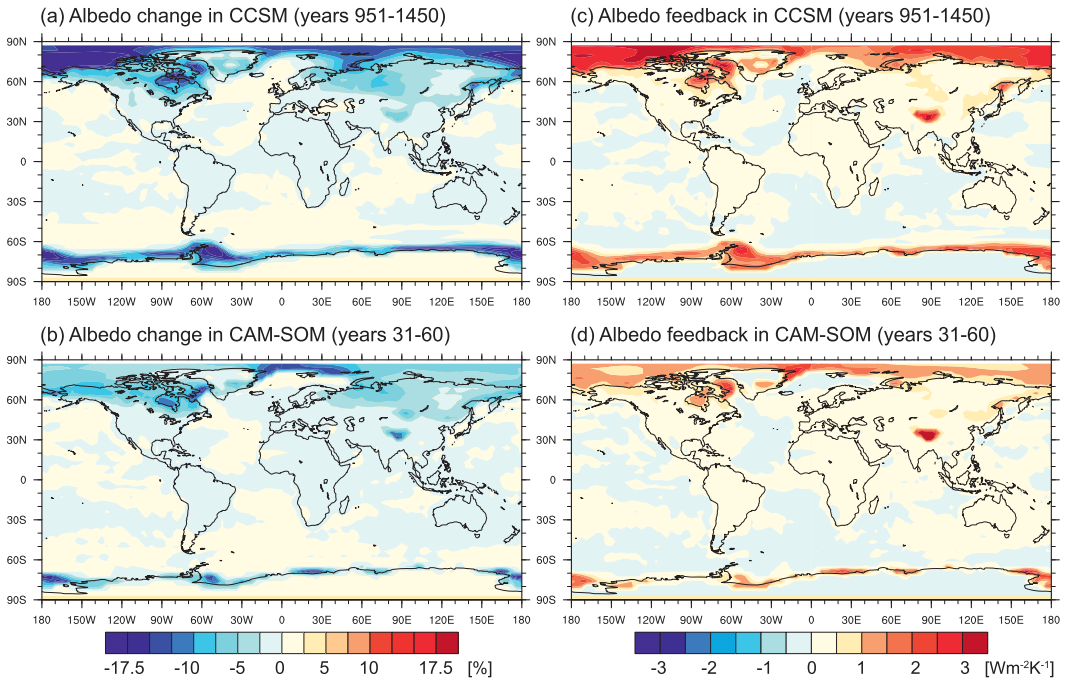

FIG. 4. (a) The 500-yr average albedo change (%) between the $8xCO_2$ and $4xCO_2$ simulations in CCSM and (b) the 30-yr average albedo change in CAM-SOM. (c),(d) Corresponding albedo feedbacks (W m^{-2} K^{-1}).

doublings is as large as or larger than (for $4xCO_2$-$2xCO_2$) the difference between successive doublings for CCSM.

d. Surface albedo feedback

The surface albedo feedback results primarily from albedo perturbations in areas experiencing changes in the extent of sea ice and snow cover. As sea ice and snow melt, they expose underlying areas, which typically have much lower albedos, leading to more SW absorption and further temperature increase. The albedo feedback decreases from 0.29 to 0.16 W m^{-2} K^{-1} in CCSM and from 0.26 to 0.09 W m^{-2} K^{-1} in CAM-SOM for the three doublings. CAM-SOM feedback values are slightly smaller than in CCSM because changes in snow and sea ice are smaller in CAM-SOM (cf. Figs. 4a and 4b). On the global average, the albedo change in CAM-SOM is only 50% of that seen in CCSM. The spatial distribution of the albedo feedback follows changes in albedo for both models (Fig. 4). However, global average hybrid feedbacks show that both the climate response and change in radiative kernel contribute approximately equally to the decrease in albedo feedback from the $2xCO_2$-$1xCO_2$ to the $8xCO_2$-$4xCO_2$ experiment (Tables 1 and 2). This behavior is supported by the zonal distribution of feedbacks in Fig. 3d, which shows a decrease in albedo feedback in the latitude bands 30°–65°N and 50°–70°S. In both hemispheres, this decrease is explained by the climate response (i.e., lines of the same color overlap) at lower latitudes. The kernel gains more importance at higher latitudes, where lines of the same color begin to diverge, while lines of the same type converge. The albedo feedback increases north of 75°N and south of 80°S. Note that changes at these high latitudes have a small contribution to the global mean, since the surface area affected as well as the amount of solar radiation received are comparatively small.

The combined effect (0.13 W m^{-2} K^{-1} in CCSM) is larger than the sum of the individual changes due to radiative kernel (0.03 W m^{-2} K^{-1}) and climate response (0.04 W m^{-2} K^{-1}), confirming the importance of nonlinearities for the albedo feedback (Shell et al. 2008). There is no overlap between any of the three feedback histograms in Fig. 2d (i.e., all differences are statistically significant).

e. Cloud feedback

Clouds have competing positive and negative feedback effects on climate. Increases in cloud cover lead to more reflection of incoming solar radiation, resulting in a negative global average SW cloud feedback if clouds increase with temperature. The CCSM SW cloud feedback is negative in the tropics and at high latitudes, and positive at midlatitudes (Fig. 3f). At the same time, more clouds also increase absorption of upwelling LW radiation. Assuming that clouds increase with temperature, this results in a positive LW cloud feedback with maxima in the tropics and high latitudes (Fig. 3e). In CCSM, these

effects combine to give a positive overall cloud feedback. The zonal distribution of the net effect follows that of the SW cloud feedback, with positive values in the midlatitudes and negative values in the tropics and high latitudes (Fig. 3g). The CCSM cloud feedback is 0.06 W m^{-2} K^{-1} for $2xCO_2$-$1xCO_2$, increasing to 0.24 W m^{-2} K^{-1} for $8xCO_2$-$4xCO_2$. In CAM-SOM cloud feedback increases from 0.05 to 0.30 W m^{-2} K^{-1}.

Going from the first to second doubling of CO_2, the increase in cloud feedback is explained by a significant decrease in the negative SW cloud feedback, occurring in the tropics to subtropics between 10° and 30°N and S as well as an increase in the positive SW cloud feedback in the NH midlatitudes. While the positive LW cloud feedback also decreases, this change is comparatively small and not recurrent. From the second to the third doubling, both the SW and LW cloud feedbacks become slightly more positive. Neither of these changes on its own is found to be recurrent. However, the combination results in a significant increase in the overall cloud feedback (see Table 1 and Figs. 2e–g).

5. Climate sensitivity and radiative forcing

We sum the Planck, lapse rate, water vapor, surface albedo, and cloud feedbacks to obtain the feedback parameter λ in Eq. (2). This sum is negative (i.e., it is dominated by stabilizing contributions from surface and air temperature changes). The residual in Eq. (2), comprising higher-order terms, is calculated explicitly by Jonko et al. (2012) and is ~10%. The negative inverse of the feedback parameter is the climate sensitivity $s = -1/\lambda$. Average climate sensitivity in CCSM increases with each doubling of CO_2, from 0.65 to 0.80 K W^{-1} m^2. The three distributions are well separated, with no overlap between adjacent histograms (Fig. 2h). These differences represent a 23% increase in average climate sensitivity between the first and third CO_2 doubling.

CAM-SOM climate sensitivities are comparable, but slightly smaller at 0.61 K W^{-1} m^2 for the $2xCO_2$-$1xCO_2$ experiment and 0.79 K W^{-1} m^2 for the $8xCO_2$-$4xCO_2$ experiment, a 30% increase. While these increases seem to be due largely to the radiative response (Table 2), complex interactions—in particular in the case of cloud feedback calculations—make such a straightforward interpretation more difficult than for the case of the noncloud feedbacks.

The increase in climate sensitivity we see in CCSM and CAM-SOM disagrees with CM09, who find that climate sensitivity decreases with each subsequent CO_2 doubling. In their model (BMRC), the increase in water vapor feedback is offset close to completely by an increase in lapse rate feedback, and the decrease in climate sensitivity is explained by a decreasing albedo feedback. In CCSM, the sum of water vapor and lapse rate feedbacks increases in magnitude rather than remaining constant, so that the increase in water vapor and cloud feedbacks outweighs the comparatively small decrease in albedo feedback.

TABLE 4. Forcing values for the three CO_2 doublings in CCSM and CAM-SOM. The adjusted forcing F_a is computed using the Gregory method (Gregory et al. 2004). Instantaneous forcing F_i is calculated as the direct effect of CO_2 using the offline radiative transfer model, and F_{CCSM} and F_{CAM} are obtained from $F = \Delta\overline{T}_{as}/s$. All forcing estimates have units of W m^{-2}.

	F_a	F_i	F_{CCSM}	F_{CAM}
$2xCO_2$-$1xCO_2$	2.90	2.54	3.38	3.61
$4xCO_2$-$2xCO_2$	3.49	3.00	3.53	3.91
$8xCO_2$-$4xCO_2$	4.31	3.59	3.72	3.77

Assuming equilibrium, we can substitute $\lambda = -1/s$ into Eq. (1) to obtain a relationship between climate sensitivity and radiative forcing, F:

$$F = \frac{\Delta\overline{T}_{as}}{s}. \tag{8}$$

Forcing values obtained for CCSM and CAM-SOM using this equation are summarized in Table 4. However, the CCSM simulations we analyze are not in equilibrium, which may bias these estimates. Therefore, we also use two alternative methods to estimate radiative forcing, which are applicable independently of whether the simulations are in equilibrium or not. The Gregory method (Gregory et al. 2004; Andrews et al. 2012) regresses radiative flux differences ($\Delta R'_{TOA}$) between two simulations against differences in surface temperature (ΔT_{as}) to yield an adjusted radiative forcing F_a. In addition to the stratospheric temperature adjustment, this forcing value also includes the direct response of clouds to the change in carbon dioxide concentrations. A drawback of this method is that it assumes linearity between radiative flux and temperature changes, which does not necessarily hold for fully coupled GCM simulations (Andrews et al. 2012). Thus, forcing estimates show a rather large dependence on how many years of model simulations are included in the regression. Following Andrews et al. (2012), we use the first 150 years of our CCSM simulations and find that the adjusted forcing increases from 2.90 W m^{-2} for $2xCO_2$-$1xCO_2$ to 4.31 W m^{-2} for $8xCO_2$-$4xCO_2$ (Fig. 5). The regression slopes in Fig. 5 do not correspond to the climate sensitivity values obtained using radiative kernels, since the estimates are based on different segments of the CCSM simulations and the slope is not constant over the length of the simulation. Additionally, we compute radiative forcing by taking

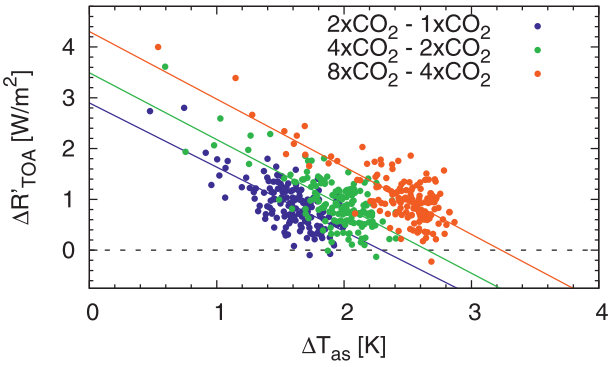

FIG. 5. Regression of global and annual average TOA radiative flux change $\Delta R'_{\mathrm{TOA}}$ against surface air temperature change $\Delta\overline{T}_{\mathrm{as}}$ for the first 150 years of CCSM simulations after an instantaneous doubling of CO_2 from baseline concentrations of 355 ppmv (blue), 710 ppmv (green), and 1420 ppmv (orange). The y intercept at $\Delta\overline{T}_{\mathrm{as}} = 0$ gives the adjusted radiative forcing F_a. Forcing values are summarized in Table 4.

the difference between TOA fluxes obtained from offline radiative transfer calculations before and after CO_2 concentrations are doubled. These forcing estimates are instantaneous, F_i, and do not take into account atmospheric adjustment (Hansen et al. 2005). Results from both methods are compared with the radiative forcing estimates from Eq. (8) in Table 4. While the absolute forcing values are sensitive to the method used to obtain them, F_a, F_i, and F_{CCSM} all increase with CO_2 baseline amount. In CAM-SOM we first see an increase between the first and second doubling and a subsequent decrease from the second to the third doubling. The prevalent positive trend of forcing is in agreement with CM09. While CM09 do not present the temperature change associated with each CO_2 doubling, we infer from forcing and climate sensitivity values in their Fig. 1 that surface temperature change must remain approximately constant, while we see an increase in surface temperature change for successive doublings. Model differences leading to this different temperature response may explain why both studies find increases in forcing, but opposite trends in climate sensitivity.

6. Discussion

We have used GCM simulations with forcings ranging from CO_2 doubling to octupling to investigate the robustness of climate sensitivity and the contributing feedbacks in both a slab ocean and a fully coupled version of the NCAR climate model. We find that, in both model versions, climate sensitivity increases with each successive doubling in CO_2 primarily due to an increase in positive water vapor and cloud feedbacks, while a decrease in positive albedo and increase in negative lapse rate feedbacks dampen this increase in sensitivity. We have decomposed the change in each feedback into contributions from radiative kernel and climate response changes. We find that while the climate response dominates the change in lapse rate and SW cloud feedbacks, radiative effects are more important for changes in water vapor and Planck feedbacks. Both play a role in the case of surface albedo and LW cloud feedbacks. Thus, climate sensitivity changes cannot be attributed mainly to one or the other factor, but are indeed the result of a combination of both.

We further see differences in the absolute magnitudes of feedbacks between the fully coupled CCSM and CAM-SOM. In some cases, for the lapse rate and SW cloud feedbacks in particular, feedbacks differ as much between the two model configurations as they do between successive doublings of CO_2. These differences can amount to as much as 40% of feedback values, as is the case for the SW cloud feedback, suggesting caution in the interpretation of studies that rely solely on slab ocean model simulations to study climate feedbacks.

Because of the long time scales necessary for adjustment of fully coupled simulations to large forcings and the associated computational expense, we have been able to use only one GCM in our analysis. The behavior of feedbacks may differ substantially for other models, as suggested by the differences between the results presented here and in CM09, for instance. This is a concern in particular in the case of feedbacks known to exhibit nonlinear behavior, such as the surface albedo feedback. However, a very limited amount of data from fully coupled millennial-length GCM simulations driven by a wide range of forcings is available. Thus, intercomparisons among several models, although desirable, are not feasible at this time.

Acknowledgments. We thank two anonymous reviewers for their constructive comments. This work was supported by NASA Headquarters under the NASA Earth and Space Science Fellowship Program, Grant "10-Earth10R-35," by the National Science Foundation under Grant ATM-0904092 and by the Office of Science (BER), U.S. Department of Energy, Cooperative Agreement DE-FC02-97ER62402. Computing resources were provided by the National Center for Atmospheric Research (NCAR) Computational and Information Systems Laboratory (CISL).

REFERENCES

Andrews, T., J. Gregory, M. Webb, and K. Taylor, 2012: Forcing, feedbacks and climate sensitivity in CMIP5 coupled atmosphere–ocean models. *Geophys. Res. Lett.,* **39,** L09712, doi:10.1029/2012GL051607.

Boer, G., and B. Yu, 2003: Climate sensitivity and response. *Climate Dyn.,* **20,** 415–429.

——, K. Hamilton, and W. Zhu, 2005: Climate sensitivity and climate change under strong forcing. *Climate Dyn.,* **24,** 685–700.

Cess, R., and G. Potter, 1987: Exploratory studies of cloud radiative forcing with a general circulation model. *Tellus,* **39,** 460–473.

Chen, C., and V. Ramaswamy, 1996: Sensitivity of simulated global climate perturbations in low cloud microphysical properties. Part I: Globally uniform perturbations. *J. Climate,* **9,** 1385–1402.

Colman, R., and B. McAvaney, 2009: Climate feedbacks under a very broad range of forcing. *Geophys. Res. Lett.,* **36,** L01702, doi:10.1029/2008GL036268.

Danabasoglu, G., 2004: A comparison of global ocean general circulation model simulations obtained with synchronous and accelerated integration methods. *Ocean Modell.,* **7,** 323–341.

——, and P. Gent, 2009: Equilibrium climate sensitivity: Is it accurate to use a slab ocean model? *J. Climate,* **22,** 2494–2499.

Forster, P., M. Blackburn, R. Glover, and K. Shine, 2000: An examination of climate sensitivity for idealised climate change experiments in an intermediate general circulation model. *Climate Dyn.,* **16,** 833–849.

Gregory, J., and Coauthors, 2004: A new method of diagnosing radiative forcing and climate sensitivity. *Geophys. Res. Lett.,* **31,** L03205, doi:10.1029/2003GL018747.

Hansen, J., and Coauthors, 2005: Efficacy of climate forcings. *J. Geophys. Res.,* **110,** D18104, doi:10.1029/2005JD005776.

Jonko, A., K. Shell, B. Sanderson, and G. Danabasoglu, 2012: Climate feedbacks in CCSM3 under changing CO_2 forcing. Part I: Adapting the linear radiative kernel technique to feedback calculations for a broad range of forcings. *J. Climate,* **25,** 5260–5272.

Raval, A., and V. Ramanathan, 1989: Observational determination of the greenhouse effect. *Nature,* **342,** 758–761.

Russell, G. L., J. R. Miller, and D. Rind, 1995: A coupled atmosphere–ocean model for transient climate change. *Atmos.–Ocean,* **33,** 683–730.

Sanderson, B., and K. Shell, 2012: Model-specific radiative kernels for calculating cloud and noncloud climate feedbacks. *J. Climate,* **25,** 7607–7624.

Shell, K., J. Kiehl, and C. Shields, 2008: Using the radiative kernel technique to calculate climate feedbacks in NCAR's Community Atmospheric Model. *J. Climate,* **21,** 2269–2282.

Soden, B., A. Broccoli, and R. Hemler, 2004: On the use of cloud forcing to estimate cloud feedback. *J. Climate,* **17,** 3661–3665.

——, I. Held, R. Colman, K. Shell, J. Kiehl, and C. Shields, 2008: Quantifying climate feedbacks using radiative kernels. *J. Climate,* **21,** 3504–3520.

Stouffer, R., 2004: Time scales of climate response. *J. Climate,* **17,** 209–217.

von Storch, H., and F. Zwiers, 1988: Recurrence analysis of climate sensitivity experiments. *J. Climate,* **1,** 157–171.

Wetherald, R., and S. Manabe, 1988: Cloud feedback processes in a general circulation model. *J. Atmos. Sci.,* **45,** 1397–1416.

Yeager, S., C. Shields, W. Large, and J. Hack, 2006: The low-resolution CCSM3. *J. Climate,* **19,** 2545–2566.

Zelinka, M., S. Klein, and D. Hartmann, 2012: Computing and partitioning cloud feedbacks using cloud property histograms. Part I: Cloud radiative kernels. *J. Climate,* **25,** 3715–3735.

Zhang, M., J. Hack, J. Kiehl, and R. Cess, 1994: Diagnostic study of climate feedback processes in atmospheric general circulation models. *J. Geophys. Res.,* **99,** 5525–5537.